Supplemental Data

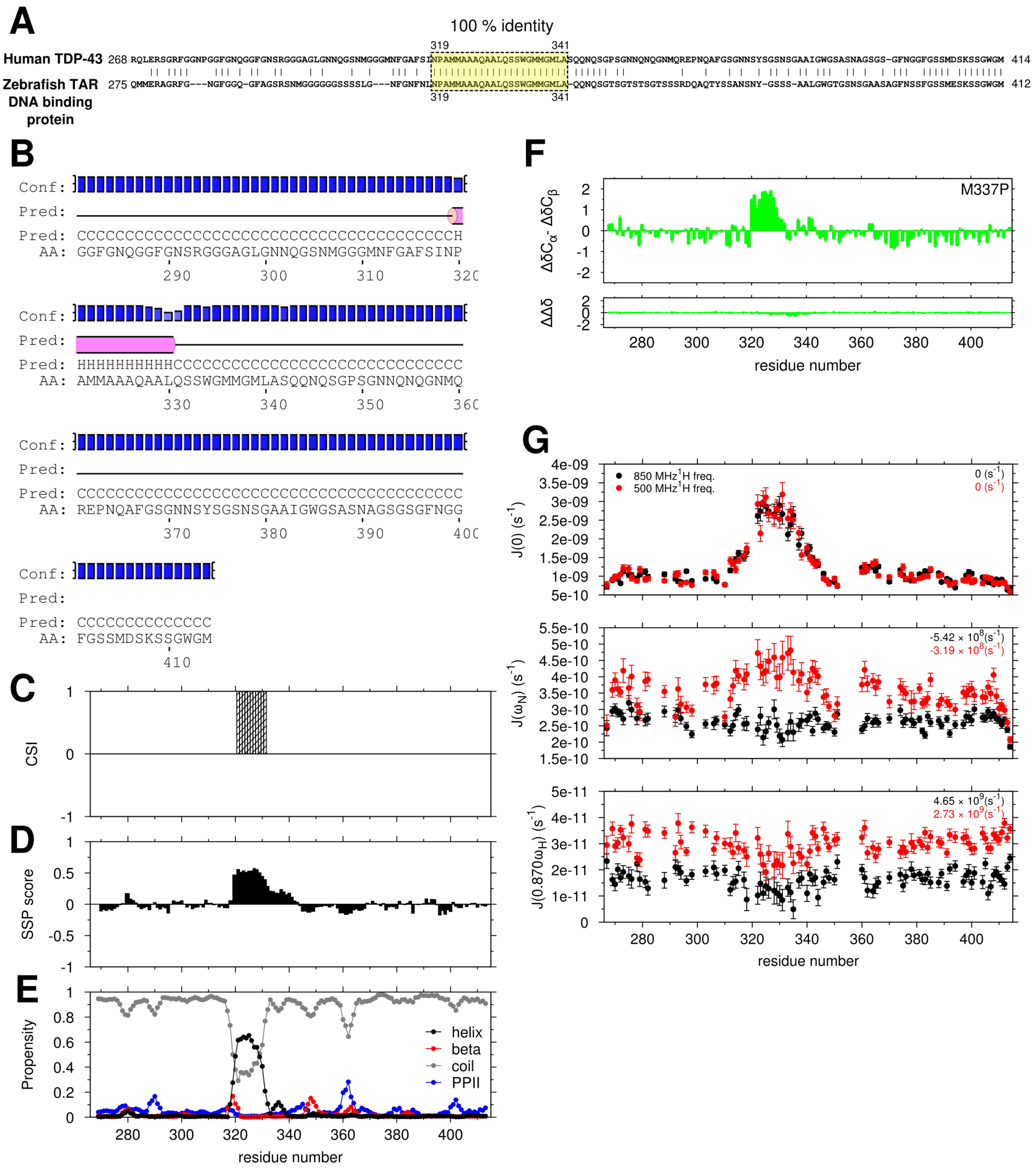

Figure S1. Structural characterization of TDP-43 C-terminal domain. Related to Figure 1 (**A**) Pairwise alignment (using EMBOSS Water with default parameters) of the C-terminal domain of human TDP-43 (Q13148) and zebrafish TAR DNA binding protein (Q802C7). Identical residues are indicated with vertical bars. Residues 319-341 in both proteins are highlighted in yellow. (**B**) PSIPRED secondary structure prediction of residues 280-414 of human TDP-43 shows α-helical structure is predicted for residues 320-330 (magenta cylinder). (**C**) Chemical shift index (CSI) calculated from experimental TDP-43 C-terminal domain chemical shifts showing helical structure (+1) for residues 321-330. (**D**) SSP scores for TDP-43 C-terminal domain showing helical propensity (positive values) from 321-340. (**E**) δ2d predicted secondary structure propensities based on experimental TDP-43 C-terminal domain chemical shifts. α-helix, β-sheet, coil, and polyproline II are illustrated by black, red, gray, and blue, respectively. (**F**) Secondary shifts for engineered variant M337P show no significant change in helical structure compared to wild type (Figure 1B). (**G**) Values of the spectral density function, $J(\omega)$, are solved for at frequencies of: 0 MHz, 86.2 MHz, 740 MHz and 0 MHz, 50.7 MHz, and 435 MHz for ^{15}N spin relaxation parameters measured at 850 MHz (black) and 500 MHz (red) ^{1}H Larmor frequency, respectively. Values of $J(0)$ and $J(\omega_N)$ are calculated assuming $J(\omega) \propto 1/\omega^2$). $J(0)$ field independence observed here is also preserved if instead it is assumed that $J(0.87\omega_H)= J(0.921\omega_H)= J(0.955\omega_H)$ (data not shown, see Methods). Data are plotted as mean ± SD.

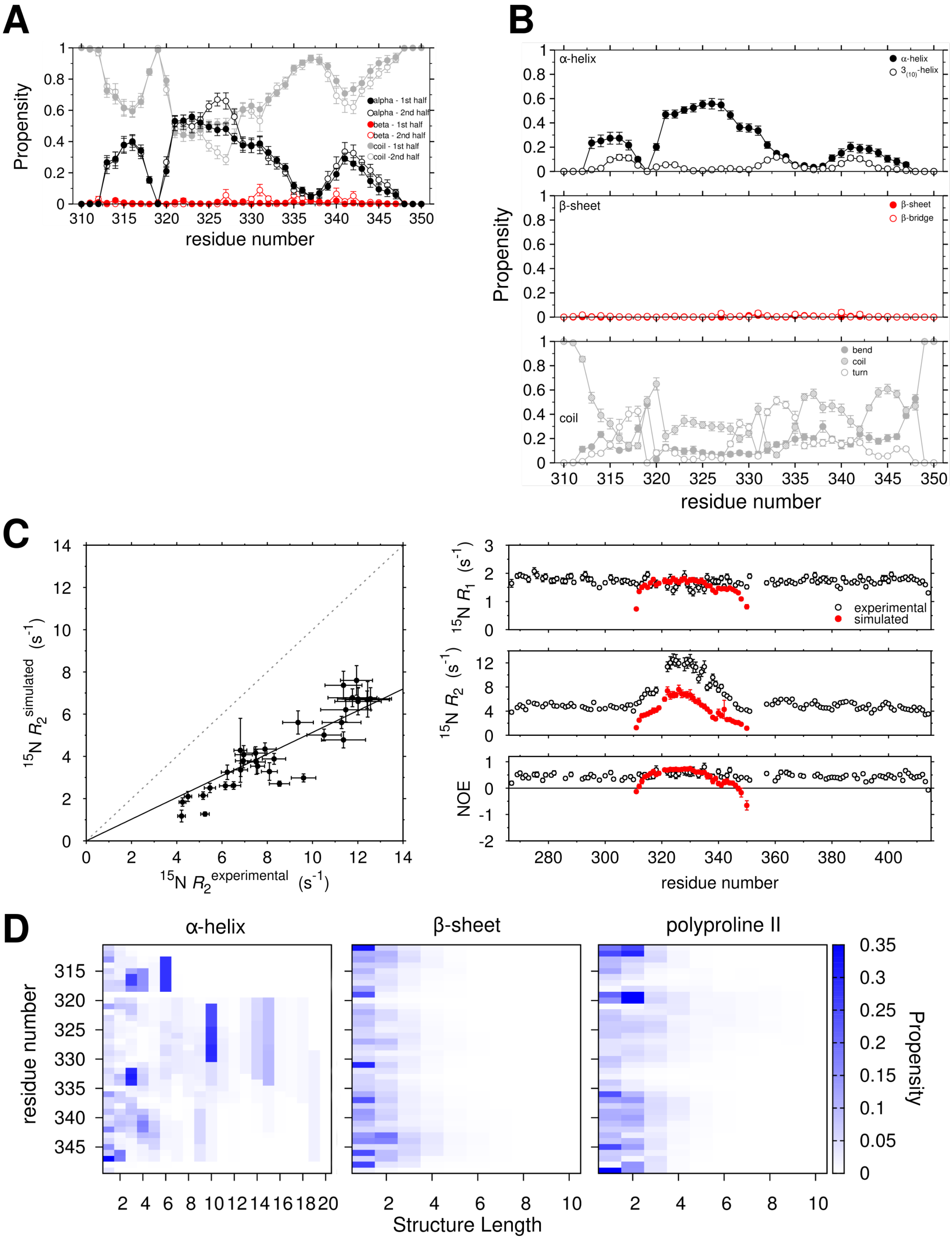
A
Propensity
residue number
alpha - 1st half
alpha - 2nd half
beta - 1st half
beta - 2nd half
coil - 1st half
coil -2nd half
B
α-helix
α-helix
$3_{(10)}$-helix
β-sheet
β-sheet
β-bridge
coil
bend
coil
turn
Propensity
residue number
C
^{15}N $R_2^{simulated}$ (s^{-1})
^{15}N $R_2^{experimental}$ (s^{-1})
^{15}N R_1 (s^{-1})
experimental
simulated
^{15}N R_2 (s^{-1})
NOE
residue number
D
α-helix
β-sheet
polyproline II
residue number
Structure Length
Propensity

Figure S2: Structural analysis of simulated conformational ensemble for TDP-43$_{310\text{-}350}$. Related to Figure 2. (**A**) Convergence of structural ensemble is demonstrated by similarity in average secondary structure propensity for first (closed circles) and second (open circles) halves of the parallel tempering simulation ensemble. (**B**) Breakdown of average per-residue secondary structure propensity into individual DSSP categories plotted in Figure 1C. Data are plotted as mean ± SD. (**C**) (Left) Correlation of experimental and simulation-derived ^{15}N R_2 values demonstrate dynamical correspondence between simulated and experimental ensembles. (Right) ^{15}N R_1, ^{15}N R_2, and heteronuclear NOE values derived from simulation (red) are overlayed with experimental values (black, reproduced from Figure 1). **(D**) Full ss-maps showing position and lengths of continuous α-helix, β-sheet, and polyproline II segments found in TDP-43$_{310\text{-}350}$ simulated ensemble based on backbone dihedral angles. Continuous α-helix structure (left, here uncropped for short residue lengths, reproduced from Figure 2B for clarity) is described in Figure 2B. No continuous β-sheet (center) or polyproline II (right) structures are found.

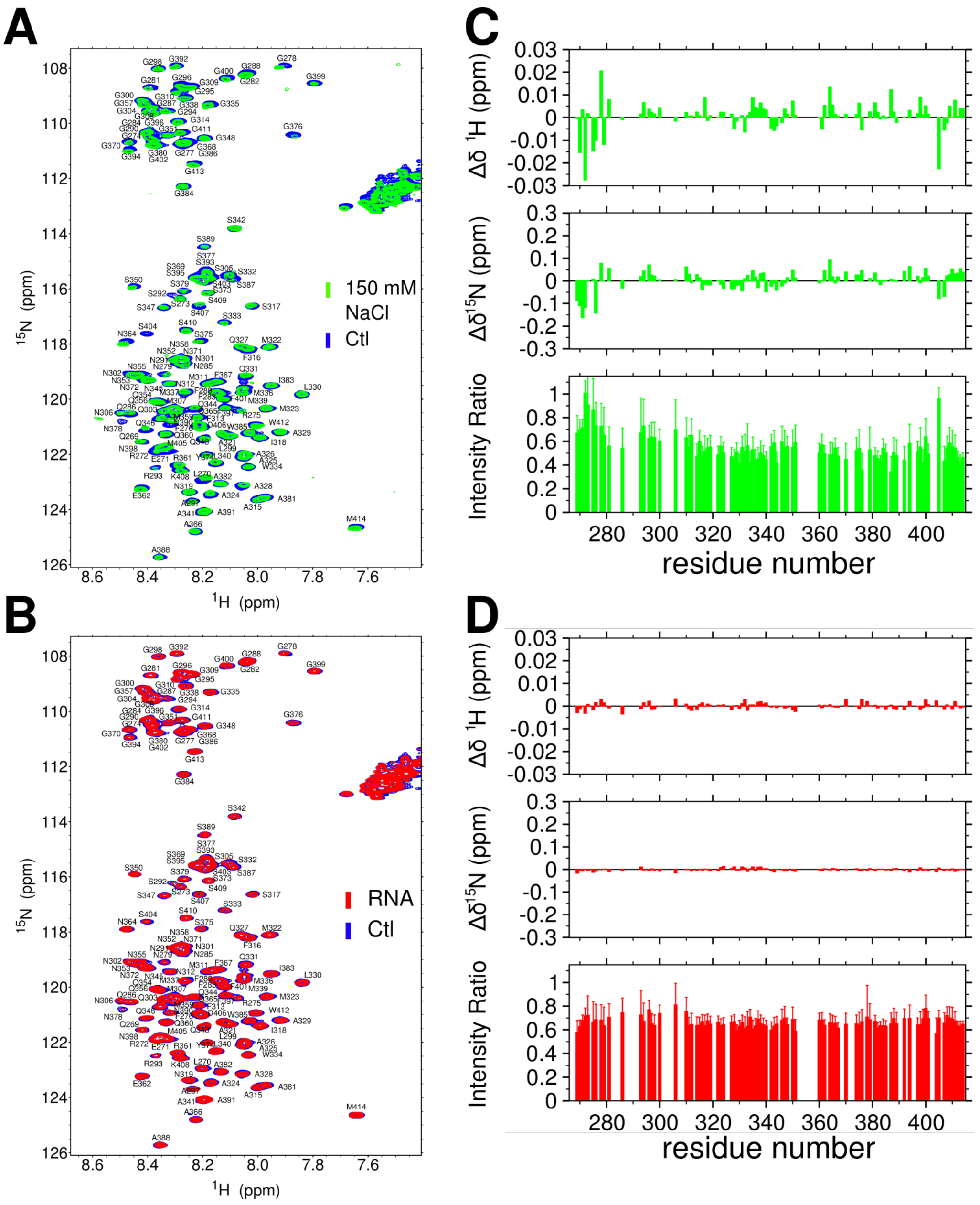

Figure S3. Salt and RNA enhance phase separation of TDP-43 C-terminal domain without global structural changes. Related to Figure 3. (**A**) Overlay of fingerprint ^{1}H-^{15}N HSQC spectra (500 MHz ^{1}H frequency for 20 µM wild type TDP-43 C-terminal domain) in NMR buffer (blue) and in NMR buffer + 150 mM NaCl (green) show small local changes but no significant change in structure. (**B**) Overlay of ^{1}H-^{15}N HSQC spectra in NMR buffer (blue, same data as in A) and in NMR buffer + 15 µg/ml yeast RNA extract (red) show no significant chemical shift differences. Quantification of spectral changes in the presence of 150 mM NaCl (**C**) and 15 µg/ml RNA (**D**) show no significant chemical shift differences, suggesting no global structural changes, but a loss in signal intensity corresponding to formation of NMR-invisible phase separated assemblies. Data are plotted as mean ± SD.

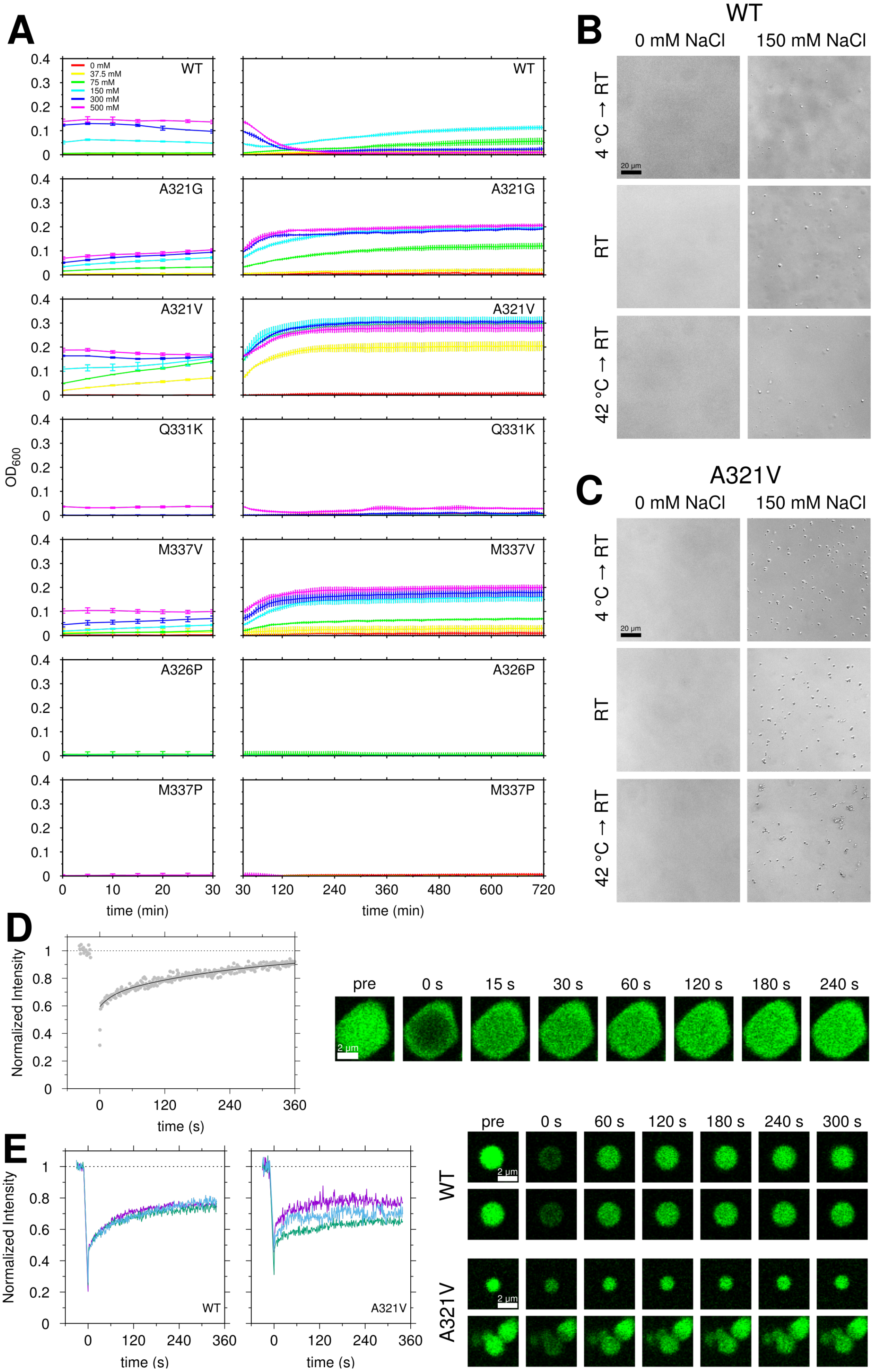A
0 mM
37.5 mM
75 mM
150 mM
300 mM
500 mM
WT
A321G
A321V
Q331K
M337V
A326P
M337P
OD600
0.4
0.3
0.2
0.1
0
0
10
20
30
time (min)
30
120
240
360
480
600
720
time (min)
B
WT
0 mM NaCl
150 mM NaCl
4 °C → RT
RT
42 °C → RT
20 µm
C
A321V
0 mM NaCl
150 mM NaCl
4 °C → RT
RT
42 °C → RT
20 µm
D
Normalized Intensity
1
0.8
0.6
0.4
0.2
0
0
120
240
360
time (s)
pre
0 s
15 s
30 s
60 s
120 s
180 s
240 s
2 µm
E
Normalized Intensity
1
0.8
0.6
0.4
0.2
0
WT
A321V
0
120
240
360
time (s)
pre
0 s
60 s
120 s
180 s
240 s
300 s
WT
A321V
2 µm

Figure S4. TDP-43 CTD liquid droplets convert to aggregates over time. Related to Figure 4. (**A**) Turbidity of 20 µM WT and mutant CTD at salt concentrations of 0 mM, 37.5 mM, 75 mM, 150 mM, 300 mM, and 500 mM was monitored at 5 minute intervals for 12 hours. DIC micrographs of 20 µM WT (**B**) and A321V (**C**) CTD at salt concentrations of 0 mM and 150 mM after a 2 minute incubation at the indicated temperature. Scale bar is 20 µm. (**D**) (*Left*) Fluorescence recovery curve for a partial liquid droplet bleach of TDP-43$_{267\text{-}414}$ A321V immediately after sample preparation. The black line represents the least squares best fit to a biexponential curve. (*Right*) Representative fluorescence images of A321V partial droplet recovery. Scale bar is 2 µm. (**E**) (*Left*) Fluorescence recovery curves for 50 µM WT (*top*) and A321V (*bottom*) after incubation at room temperature for 1 hour. (*Right*) Representative images illustrating fluorescence recovery at indicated time points. Scale bar is 2 µm. Data are plotted as mean ± SD.

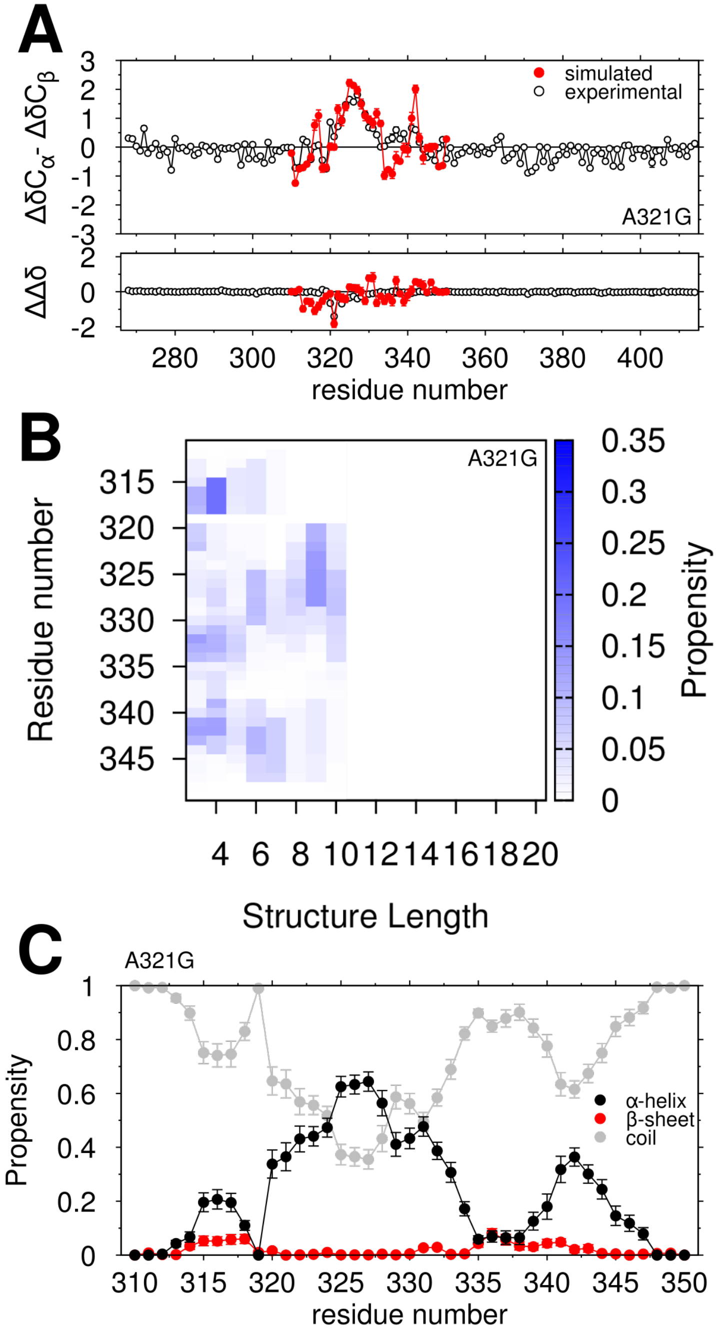

Figure S5. Structural characteristics of the TDP$_{310\text{-}350}$ A321G structural ensemble. Related to Figure 5. (**A**) (Top) Secondary shifts measured for 20 μM CTD A321G (black, open circles, reproduced from Figure 4) overlayed with calculated secondary shifts for TDP-43$_{310\text{-}350}$ A321G (red). (Bottom) Secondary shift differences between wild type and A321G (ΔΔδ) are similar, especially the marked decrease near the mutation position 321, suggesting that TDP-43$_{310\text{-}350}$ A321G captures the loss of α-helical structure observed experimentally. (**B**) Decreased helical structure population and length compared to wild type (see Figure 2B) are observed for simulated A321G ensemble. (**C**) Secondary structure propensity for the TDP-43$_{310\text{-}350}$ A321G ensemble highlights a reduction in α-helical structure for residues 320-325 with respect to residues 326-329. Simulation data are plotted as mean ± SEM.

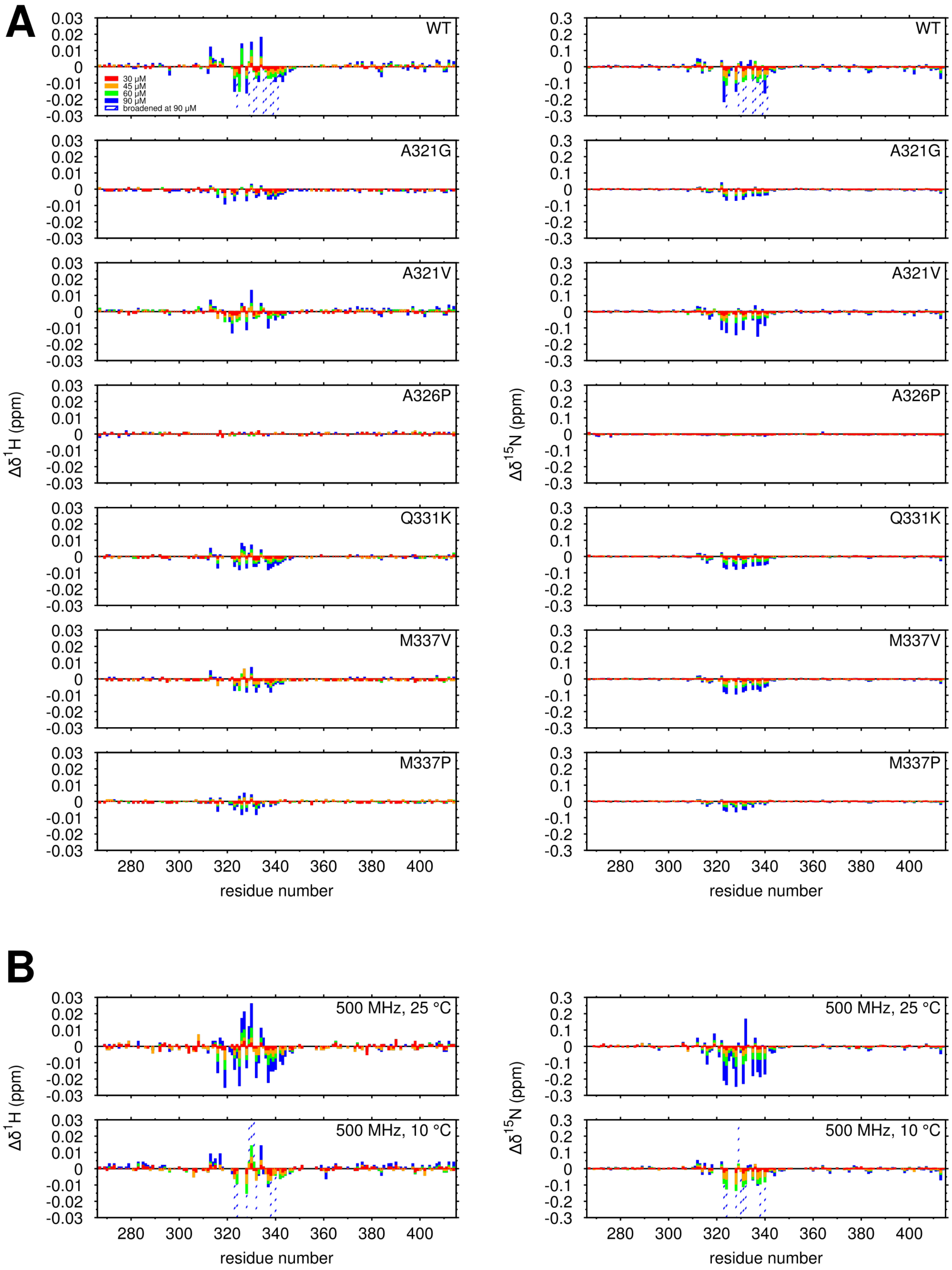

Figure S6. Helix-mediated interactions are suppressed by TDP-43 ALS-associated and structure-breaking mutants. Related to Figure 6. (A) Concentration-dependent ^{1}H and ^{15}N chemical shift differences measured for WT and mutant TDP-43 C-terminal domain at 850 MHz ^{1}H frequency. ^{15}N chemical shift deviations as a function of concentration (summarized in Figure 5B) show a similar pattern but different amplitudes for wild type and mutants, suggesting a similar assembled structure is populated to differing extents. (**B**) Concentration-dependent ^{1}H and ^{15}N chemical shift differences measured for WT TDP-43 C-terminal domain measured at 500 MHz ^{1}H field, 25 °C (top) or 10 °C (bottom) are similar to those measured at 850 MHz ^{1}H field (Figure 5B and S4A), suggesting the complex is populated similarly at both temperatures and probed well at both fields.

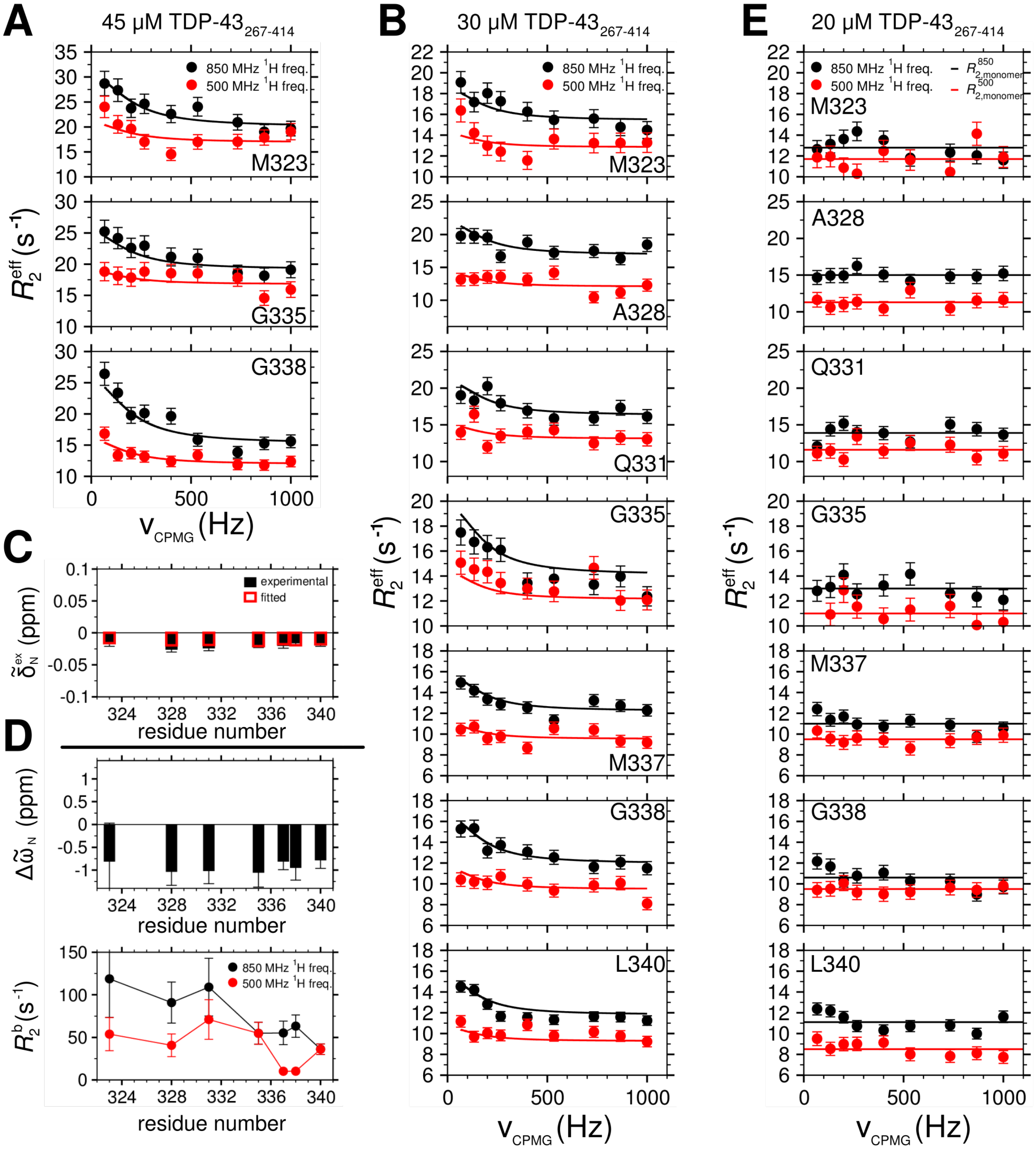

Figure S7. Relaxation dispersion profiles and exchange induced shifts probe exchange between monomeric and assembled forms of TDP-43 C-terminal domain. Related to Figure 7. (**A**) Best-fit ^{15}N CPMG dispersion profiles for residues M323, G335, and G338 recorded for 45 µM TDP-43 C-terminal domain at 850 MHz and 500 MHz ^{1}H frequencies to the two-state assembly model described in the main text. Fits for residues A328, Q331, M337, and L340, as well as fitted exchange parameters can be found in Figure 6, panels B-E. (**B**) Best-fit ^{15}N CPMG dispersion profiles for residues M323, A328, Q331, G335, M337, G338, and L340 measured for 30 µM TDP-43 C-terminal domain at 850 MHz and 500 MHz ^{1}H frequencies to the two-state assembly model described in the main text. Data are plotted as mean ± SD. (**C**) Exchange-induced chemical shifts and (**D**) exchange parameters $\Delta\tilde{\omega}_N$ (top) and R_2^b (bottom) extracted from the dispersion profiles presented in panel B for 30 μM TDP-43 C-terminal domain. (**E**) Lack of observed ^{15}N CPMG relaxation dispersion for residues M323, A328, Q331, G335, M337, G338, and L340 at 20 μM TDP-$43_{267\text{-}414}$ at 850 MHz and 500 MHz ^1H frequencies. This observation suggests these values can be used as the monomeric reference values for R_2^a (solid lines). Data are plotted as mean ± SD.

Supplemental Movie Legend

Movie S1. Liquid-liquid phase separated TDP-$43_{267\text{-}414}$. Related to Figure 3. Confocal microscopy of a 20 μl drop of 50 μM TDP-43 C-terminal domain + 5 nM Dylight488-NHS-labeled TDP-43 C-terminal domain in 150 mM NaCl 20 mM MES pH 6.1. Micron sized phase separated TDP-43 C-terminal domain assemblies are seen falling down onto the glass coverslip surface and fusing with liquid droplets present in the current focal plane. Movie is 300 seconds of real time. Scale bar is 5 μm.

Supplemental Experimental Procedures

Cloning, expression, and purification of TDP-43$_{267\text{-}414}$ and ALS-associated mutant variants

The human TDP-43 protein sequence, with an additional N-terminal His tag and TEV protease cleavage site(Peti and Page, 2007), was codon optimized for recombinant expression in *Escherichia coli* and synthesized by DNA2.0. To generate the TDP-43 C-terminal domain (TDP-43$_{267\text{-}414}$) construct, the nucleotide sequence encoding residues 267-414 was amplified by PCR with the primers TDP-43-CTD-Forward (5′-TGACATATGAACCGCCAACTGGAA-3′) and TDP-43-CTD-Reverse (5′-TCACTCGAGTTACATGCCCCAACC-3′) and ligated into the *Nde*I and *Xho*I restriction sites resulting in addition of a GH sequence at the N-terminus after TEV cleavage. ALS-associated missense mutations and engineered helix-breaking mutations were introduced by site-directed mutagenesis (Quikchange).

WT or mutant TDP-43$_{267\text{-}414}$ proteins were overexpressed in *E. coli* BL21 Star (DE3) (Life Technologies). Uniform ^{15}N and ^{15}N/^{13}C labeling of TDP-43$_{267\text{-}414}$ was achieved by overexpression in M9 minimal media supplemented with ^{15}N ammonium chloride and/or ^{13}C glucose as the sole sources of nitrogen and carbon, respectively. Cell pellets were resuspended in lysis buffer (20 mM Tris-Cl, 500 mM NaCl, 10 mM Imidazole, 1 mM DTT, pH 8.0) supplemented with one tablet EDTA-free protease inhibitor cocktail per 40 ml lysis buffer (Roche Diagnostics). Cells were lysed with an EmulsiFlex-C3 (Avestin), after which inclusion bodies were pelleted by centrifugation at 20,000 ×g for 1 hour. Inclusion bodies were resuspended in denaturing binding buffer (20 mM Tris-Cl, 500 mM NaCl, 10 mM Imidazole, 1 mM DTT, 8 M urea, pH 8.0), and centrifuged again at 20,000 ×g for 1 hour to pellet any remaining insoluble cell debris. Protein was bound to a 5 ml Histrap HP column (GE Healthcare), and eluted with a linear gradient of denaturing buffer with imidazole (20 mM Tris-Cl, 500 mM NaCl, 500 mM imidazole, 1 mM DTT, 8 M urea, pH 8.0). TDP-43$_{267\text{-}414}$-containing fractions were pooled and desalted with a HiPrep 26/60 Desalting Column (GE Healthcare) into TEV-Cleavage Buffer (20 mM MES, pH 5.5). His-tagged TEV protease(Tropea et al., 2009) was added to a final concentration of 30 µg/ml in order to cleave the N-terminal His tag, and the resulting mixture was passed over the 5 ml Histrap HP column in order to remove the cleaved histidine-tag, histidine-tagged TEV protease, and any uncleaved TDP-43$_{267\text{-}414}$. Purified TDP-43$_{267\text{-}414}$ was buffer exchanged into denaturing buffer pH 6.1 (20 mM MES, 8 M urea, pH 6.1), flash frozen and stored at -80 °C. Frozen samples were thawed on ice and desalted into the NMR buffer (20 mM MES, 10% D_2O, pH 6.1) with a 0.5 ml Zeba Spin Desalting column (Thermo Scientific) or 5 ml Zeba Desalting Cartridge (Thermo Scientific) according to the manufacturer's instructions.

For paramagnetic relaxation enhancement (PRE) measurements, TDP-43$_{267\text{-}414}$ constructs including a single engineered cysteine residue substitution at S273, S317 or S387 were conjugated to the paramagnetic stabilized nitroxide radical compound (1-Oxyl-2,2,5,5-tetramethyl-Δ3-pyrroline-3-methyl) Methanethiosulfonate (MTSL) or (1-Acetoxy-2,2,5,5-tetramethyl-δ-3-pyrroline-3-methyl) Methanethiosulfonate (AcMTSL, used as a diamagnetic control) (Toronto Research Chemicals). Briefly, 30-50 µM TDP-43$_{267\text{-}414}$ S317C or S387C was incubated in 20 mM Tris, pH 8.0, 150 mM NaCl, 8 M urea with 1 mM MTSL or AcMTSL for 1 hour at room temperature. Excess unconjugated label was removed with a HiPrep 26/60 Desalting Column (GE Healthcare), and the protein samples were concentrated, flash frozen, and stored at -80 °C.

Turbidity characterization

WT TDP-43$_{267\text{-}414}$ and mutant variants were diluted to a final concentration of 20 µM in a 100 µl volume of 20 mM MES, pH 6.1 supplemented with 10 µM Thioflavin T (Sigma) and 0 mM, 50 mM, 150 mM, 300 mM, or 600 mM NaCl or torula yeast RNA extract (Sigma) at 3 µg/ml, 15 µg/ml, 30 µg/ml, 45 µg/ml, 60 µg/ml, or 90 µg/ml. Turbidity was assessed by measuring the optical density at 600 nm. Measurements were recorded in triplicate in 96-well black plates using a SpectraMax M5 Microplate reader.

Morphological changes to WT, A321G, A321V, and M337V samples were monitored over time using DIC micrographs of 20 µl (20 µM) protein sample spotted on a glass coverslip. Images were recorded at 1 hour intervals over a 3 hour period. All DIC micrographs were acquired on a Zeiss Axiovert 200M with a 40 × objective with a numerical aperture of 0.75. Images were process with ImageJ.

Liquid-liquid phase separation reversibility

WT TDP-43$_{267-414}$ and mutant variants were diluted to a final concentration of 20 µM in 20 mM MES, pH 6.1, 1 mM DTT supplemented with 0 mM, 75 mM, or 150 mM NaCl in a clear 96-well plate and sealed with optical film. Sample temperature was adjusted according to the following schedule: room temperature (RT), 4 °C, RT, 42 °C, RT, and 4 °C by incubation for 2 minutes at each temperature in pre-equilibrated water baths. Turbidity was measured in triplicate as described above.

Morphological changes to WT and A321V protein samples as a result of temperature cycling were monitored using DIC micrographs of 20 µl (20 µM) protein sample spotted on glass coverslips. Proteins samples were prepared as described above, and subjected to one of the three following temperature cycles: 4 °C to RT, RT to RT, or 42 °C to RT by incubation at each temperature for 2 minutes in pre-equilibrated water baths. Images were acquired and processes as described above.

Fluorescence Recovery after Photobleaching

Fluorescence recovery after photobleaching was performed on droplets ≥ 2 µm in diameter, with bleach areas ≤ 6 µm in diameter. An image time series was acquired with 1 second intervals on a Zeiss LSM 710 confocal microscope with a 40 × W objective with a numerical aperture of 1.2. Images were processed with ImageJ. After background intensity was subtracted, fluorescence intensities were normalized to unbleached, reference droplets in order to account for any illumination changes during acquisition. Partial droplet fluorescence recovery data were fit to a double exponential growth curve using Gnuplot fitting routines.

NMR Spectroscopy

NMR spectra were processed with NMRPipe (Delaglio et al., 1995) and analyzed with NMRFAM-Sparky (Lee et al., 2015). Backbone amide resonance assignments for WT and mutant TDP-43$_{267-414}$ were obtained using standard Bruker three dimensional triple-resonance experiments: HNCACB, CBCA(CO)NH, HNCO, and HN(CA)CO as described previously(Burke et al., 2015). Secondary chemical shifts ($\Delta\delta C\alpha$-$\Delta\delta C\beta$) were calculated as follows: $\Delta\delta C\alpha$-$\Delta\delta C\beta$ = ($\delta C\alpha_{exp}$-$\delta C\alpha_{ref}$) - ($\delta C\beta_{exp}$-$\delta C\beta_{ref}$), where $\delta C\alpha_{exp}$ and $\delta C\beta_{exp}$ are the experimentally measured Cα and Cβ chemical shifts, and $\delta C\alpha_{ref}$ and $\delta C\beta_{ref}$ are the calculated Cα and Cβ random coil reference chemical shifts computed using the Poulsen IDP/IUP random coil chemical shifts calculator using default parameters and the experimental temperature (http://spin.niddk.nih.gov/bax/nmrserver/Poulsen_rc_CS/)(Kjaergaard et al., 2011; Kjaergaard and Poulsen, 2011), respectively.

Chemical shift perturbations were quantified by recording the ^{1}H and ^{15}N chemical shifts of WT TDP-43$_{267-414}$ and mutant variants at concentrations of 20 µM (used as a monomeric reference), 30 µM, 45 µM, 60 µM, and 90 µM using a series of ^{1}H-^{15}N HSQCs recorded at 850 MHz ^{1}H frequency, 10 °C or 500 MHz ^{1}H frequency, 10 °C and 25 °C. Each ^{1}H-^{15}N HSQC recorded at 850 MHz ^{1}H frequency was acquired with 200* and 2048* complex pairs in the indirect ^{15}N and direct ^{1}H dimensions, with corresponding acquisition times of 122 ms and 201 ms, and sweep widths of 19.0 ppm and 12.0 ppm centered at 116.5 ppm and 4.7 ppm, respectively. Each ^{1}H-^{15}N HSQC recorded at 500 MHz ^{1}H frequency was acquired with 200* and 1536* complex pairs in the indirect ^{15}N and direct ^{1}H dimensions, with corresponding acquisition times of 208 ms and 219 ms, and sweep widths of 19.0 ppm and 14.0 ppm centered at 116.5 ppm and 4.7 ppm, respectively. Chemical shift differences for ^{1}H and ^{15}N were quantified by subtracting the the chemical shift value for each ^{1}H-^{15}N crosspeak of the 20 µM reference sample from the respective crosspeak in the high-concentration samples.

Cα chemical shift differences between 60 µM and 20 µM TDP-43$_{267-414}$ were quantified using standard Bruker 3D HNCA experiments. Each experiment was acquired at 850 MHz ^{1}H frequency with 50* × 39* × 2048* complex pairs in the indirect ^{13}C, indirect ^{15}N, and direct ^{1}H dimensions, with corresponding acquisition times of 10 ms, 23 ms, and 186 ms and sweep widths of 23 ppm, 20 ppm, and 13 ppm centered around 51.5 ppm, 116.5 ppm, and 4.7 ppm, respectively.

^{15}N R_1, ^{15}N R_2, and (^{1}H)^{15}N heteronuclear NOE experiments were measured for a 20 μM TDP-43$_{267\text{-}414}$ sample at 850 MHz and 500 MHz ^{1}H frequencies using standard pulse sequences (hsqct1etf3gpsitc3d, hsqct2etf3gpsitc3d, hsqcnoef3gpsi). ^{15}N R_1 and ^{15}N R_2 experiments recorded at 850 MHz ^{1}H frequency were acquired with 150* and 2048* complex pairs in the indirect ^{15}N and direct ^{1}H dimensions, corresponding acquisition times of 92 ms and 201 ms, and sweep widths of 19.0 ppm and 12.0 ppm centered at 116.5 ppm and 4.7 ppm, respectively. ^{15}N R_1 and ^{15}N R_2 experiments were acquired at 500 MHz ^{1}H frequency with 128* and 1536* complex pairs in the indirect ^{15}N and direct ^{1}H dimensions, corresponding acquisition times of 126 ms and 237 ms, and sweep widths of 20.0 ppm and 13.0 ppm centered at 116.5 ppm and 4.7 ppm, respectively. Each ^{15}N R_1 experiment comprises seven ^{15}N R_1 relaxation delays: 100 ms, 200 ms, 300 ms, 400 ms, 600 ms, 800 ms, and 1000 ms. Each ^{15}N R_2 experiment comprises six interleaved ^{15}N R_2 relaxation delays with a B_1 field of 556 Hz: 16.4 ms, 49.3 ms, 82.1ms, 114.9 ms, 164.2 ms, and 213.5 ms at 850 MHz ^{1}H frequency and 15.8 ms, 31.5 ms, 63.0 ms, 126.1 ms, 189.1 ms, and 252.2 ms at 500 MHz ^{1}H frequency. (^{1}H)^{15}N heteronuclear NOE experiments comprise interleaved proton saturation sequences and reference sequences without proton saturation with a recycle delay of 5 s. (^{1}H)^{15}N het-NOEs recorded at 850 MHz ^{1}H frequency were acquired with 62* and 2048* complex pairs in the indirect ^{15}N and direct ^{1}H dimensions, corresponding acquisition times of 38 ms and 201 ms, and sweep widths of 19 ppm and 12 ppm centered around 116.5 ppm and 4.7 ppm, respectively. (^{1}H)^{15}N het-NOEs recorded at 500 MHz ^{1}H frequency were acquired with 250* and 1536* complex pairs in the indirect ^{15}N and direct ^{1}H dimensions, corresponding acquisition times of 124 ms and 237 ms, and sweep widths of 20 ppm and 13 ppm centered around 116.5 ppm and 4.77 ppm, respectively.

^{15}N Carr Purcell Meiboom Gill (CPMG) relaxation dispersion experiments(Wang et al., 2001) were used to measure effective transverse relaxation rates, ^{15}N R_2^{eff}, as a function of applied radiofrequency field, B_1 to interrogate the μs-ms timescale conformational exchange of the TDP-43$_{267\text{-}414}$. Samples comprised 45 μM, 30 μM, and 20 μM protein concentration. Each ^{15}N CPMG relaxation dispersion experiment comprises 10 interleaved ^{15}N B_1 fields: 0 Hz, 67 Hz, 133 Hz, 200 Hz, 267 Hz, 400 Hz, 533 Hz, 733 Hz, 866 Hz, and 1000 Hz with a total CPMG relaxation delay of 60 ms. Each ^{15}N CPMG experiment at 850 MHz ^{1}H frequency was acquired with 128* and 2048* complex pairs in the indirect ^{15}N and direct ^{1}H dimensions, with corresponding acquisition times of 74 ms and 172 ms, and sweep widths of 19 ppm and 12 ppm centered around 116.5 ppm and 4.7 ppm, respectively. Each ^{15}N CPMG experiment at 500 MHz ^{1}H frequency was acquired with 100* and 1536* complex pairs in the indirect ^{15}N and direct ^{1}H dimensions, with corresponding acquisition times of 197 ms and 219 ms, and sweep widths of 20 ppm and 14 ppm centered around 116.5 ppm and 4.7 ppm, respectively.

$^3J_{HNH\alpha}$ scalar couplings were measured using a standard Bruker pulse sequence (hnhagp3d) at 500 MHz ^{1}H frequency. $^3J_{HNH\alpha}$ values were calculated as described by Vuister and Bax(Vuister and Bax, 1993).

Intermolecular PREs were measured on a 20 μM WT TDP-43$_{267\text{-}414}$ sample supplemented with 5 μM spin-label-conjugated (MTSL or AcMTSL) TDP-43$_{267\text{-}414}$ in NMR buffer. For control experiments with a detached spin label, 5 μM MTSL (or AcMTSL) was added to samples of 20 μM ^{15}N WT TDP-43$_{267\text{-}414}$. Backbone amide proton transverse relaxation rate constant, ^{1}H$_N$ R_2, were measured(Fawzi et al., 2010) at 850 MHz ^{1}H frequency for paramagnetic and diamagnetic samples, with 128* and 1536* complex pairs in the ^{15}N indirect and ^{1}H direct dimensions, corresponding acquisition times of 74.3 ms and 172 ms, and sweep widths of 20 ppm and 10.5 ppm centered around 116.5 ppm and 4.7 ppm, respectively. Each ^{1}H$_N$ R_2 experiment comprised eight interleaved ^{1}H$_N$ R_2 relaxation delays: 0.2 ms, 10 ms, 10 ms, 20 ms, 40 ms, 60 ms, 60 ms, and 90 ms. PRE rates (Γ_2) rates were obtained from the difference in ^{1}H R_2 rates for the paramagnetic and diamagnetic samples ^{1}H$_N$ $R_{2,\text{para}}$ - ^{1}H$_N$ $R_{2,\text{dia}}$.

Reduced spectral density mapping

Discrete spectral density function values at frequencies 0, ω_N, and 0.870ω_H were evaluated for ^{15}N spin relaxation data acquired at 850 MHz and 500 MHz ^{1}H Larmor frequencies using reduced spectral density mapping (Farrow et al., 1995), with the assumption that for high frequency (i.e. ω_H) terms either $J(\omega) \propto (1/\omega^2)$ or $J(0.87\omega_H) = J(0.921\omega_H) = J(0.955\omega_H)$. Errors were estimated using a Monte Carlo procedure with 1000 simulated data sets.

Normalized chemical shift differences

^{15}N chemical shift differences ($\Delta\delta$) for WT and mutant TDP-43$_{267\text{-}414}$ at 30 μM, 45 μM, 60 μM, and 90 μM (see above) were normalized to 60 μM wild type $\Delta\delta$ ^{15}N by least squares optimization of the following equation:

$$\sum_{i=267}^{414}\left(\frac{\Delta\delta_{i,\exp}}{\alpha}-\Delta\delta_{i,\mathrm{ref}}\right) \qquad \text{(Equation S1)}$$

in which α is a global scaling parameter and $\Delta\delta_{i,\mathrm{exp}}$ and $\Delta\delta_{i,\mathrm{ref}}$ are the residue-specific ^{15}N chemical shift differences of the WT or mutant TDP-$43_{267\text{-}414}$ at all sample concentrations and the ^{15}N chemical shift differences for the reference concentration (60 μM WT TDP-$43_{267\text{-}414}$), respectively.

Quantification of μs-ms exchange parameters

^{15}N R_2^{eff} rates obtained with ^{15}N CPMG experiments for 45 μM or 30 μM TDP-$43_{267\text{-}414}$ at 850 MHz and 500 MHz ^{1}H frequencies were fit simultaneously with exchange induced chemical shifts ($\Delta\delta^{\mathrm{ex}}$) at 850 MHz to a two state model of chemical exchange described previously(Libich et al., 2013). The effective in-phase/anti-phase transverse relaxation rate constant of free monomeric TDP-43, ^{15}N R_2^{a} was obtained from the average ^{15}N R_2^{eff} for the 20 μM, monomeric reference sample across all CPMG fields. Error estimates for the effective transverse relaxation rates in the assembled state, ^{15}N R_2^{b}, the chemical shift difference between the monomeric and assembled states, $\Delta\tilde{\omega}_{\mathrm{N}}$, the exchange rates, k_{ex}, and the population of the assembled state, p_{B}, were obtained from Monte Carlo sampling with 10 independent fits.

Simulation Methods

We perform parallel tempering metadynamics in well-tempered ensembles (PTMetaD-WTE) simulations of 310-350 fragment of TDP-43 (TDP-$43_{310\text{-}350}$) in aqueous solution, using GROMACS-4.6.7(Berendsen et al., 1995; Hess et al., 2008) and Plumed 2.1(Bonomi et al., 2009). In standard parallel tempering simulations, a number of replicas of the system are simulated at different temperatures(Sugita and Okamoto, 1999). Exchanges between adjacent temperature replicas are attempted periodically and are accepted based on a Metropolis criterion. The enhanced sampling in standard parallel tempering simulations is achieved by periodic exchanges with high temperature replicas, which can overcome barriers in the potential energy landscape. However, the number of parallel simulation replicas required for sufficient energy overlap to generate efficient exchange increases rapidly with system size, needing many dozens of replicas for simulations of disordered proteins. To help overcome this problem, we combined metadynamics and parallel tempering as described previously(Bussi et al., 2006). Here, potential energy of the system is introduced as a collective variable to bias in a well-tempered metadynamics scheme (well-tempered ensemble or WTE)(Bonomi and Parrinello, 2010). WTE amplifies potential energy fluctuations maintaining the same average energy, thereby reducing the number of replicas necessary for a sufficient exchange acceptance percentage(Bonomi and Parrinello, 2010; Deighan et al., 2012). Here, sixteen replicas were used within a temperature range of 300-520 K and exchanges between adjacent replicas were attempted every 1 ps. Temperatures of the replicas were adjusted, initially based on geometric spacing between 300 K and highest temperature of interest, to obtain uniform acceptance probability (of approximately 35%) between all adjacent replica pairs(Prakash et al., 2011). All the replicas were started from unstructured configurations of the peptide. For the first 50 ns of the run, WTE was turned on for all replicas, except the 300 K replica(Papaleo et al., 2014; Sutto and Gervasio, 2013). During run extension, the energy bias accumulated in the first 50 ns is loaded as a static bias. 1.2 and 500 kJ/mol gaussian height and width were used, respectively, together with a deposition frequency of every 4 ps and a bias factor of 36. The peptide was simulated for 200 ns per replica. Analysis of the last 150 ns of 300 K trajectory is presented in results section.

Amber ff03ws protein force field(Best et al., 2014) was used in combination with TIP4P/2005 water model(Abascal and Vega, 2005) with optimized protein-water interactions to improve protein-protein interaction strengths and the size of unfolded and disordered peptides(Best et al., 2014). One copy of the TDP-$43_{310\text{-}350}$ monomer was solvated in a truncated octahedron box with 6.5 nm spaced faces (6775 water molecules). Electrostatic interactions were calculated using the particle-mesh Ewald method(Essmann et al., 1995) with a real space cutoff distance of 0.9 nm. A 1.2 nm cutoff distance was used for the van der Waals interactions. Systems were propagated using stochastic Langevin dynamics with a friction coefficient of 1 ps^{-1}.

NMR chemical shift deviations in the equilibrium ensemble are calculated using an empirical chemical shift deviation prediction algorithm, SPARTA+(Shen and Bax, 2010). $^3J_{\mathrm{HNH}\alpha}$ scalar coupling constants are computed using the Karplus equation,

$J(\phi) = A\,cos^2(\phi - 60) + B\,cos(\phi - 60) + C$ (Equation S2)

where ϕ torsion angles are evaluated using the “ensemble” parameter set from Vogeli et al.(Vogeli et al., 2007). Secondary structure content of the peptide was assigned by using DSSP algorithm(Kabsch and Sander, 1983) and results were grouped into three major classes of secondary structures(Rost and Sander, 1993), alpha (α-helix+3(10)-helix), beta (β-sheet+β-bridge) and coil (everything else). Backbone torsion angles (ϕ,ψ) were also computed to determine average per-residue fraction of α-helix, β-sheet, and polyproline-II sampled in Ramachandran map, classifying the (ϕ,ψ) space as follows: α-helix, $-160^\circ<\phi<-20^\circ$ and $-120^\circ<\psi<50^\circ$; β-sheet, $-180^\circ<\phi<-90^\circ$ and $50^\circ<\psi<240^\circ$ or $160^\circ<\phi<180^\circ$ and $110^\circ<\psi<180^\circ$; polyproline-II, $-90^\circ<\phi<-20^\circ$ and $50^\circ<\psi<240^\circ$; others, everything else(Best et al., 2008). Based on this definition, secondary structure maps showing the position and length of secondary structure elements in the peptide(Iglesias et al., 2013) were calculated. Structure-based clustering of the equilibrium ensemble were performed using GROMOS algorithm(Daura et al., 1999) based on backbone root-mean-square-distance (RMSD) criteria.

To analyze the NMR relaxation parameters from the simulation data, we also perform constant temperature molecular dynamics simulations of the TDP-43$_{310\text{-}350}$ monomer using the same run parameters as above (without enhanced sampling), also in NVT ensemble (T=300 K). 12 independent MD simulations are performed for 12 randomly selected initial configurations from the equilibrium ensemble (see above). Each independent set is run for 200 ns, yielding a total of 2.4 μs simulation time. Results from dynamics trajectories are presented as averages over 12 independent simulations, and errors are the standard error calculated from the deviation between 12 simulations. For ^{15}N NMR relaxation rate constants calculations, N-H bond vector autocorrelation for each residue of each trajectory is extracted for the ensemble averaged second order Legendre polynomial autocorrelation function. Each autocorrelation decay curve is then fitted to a double exponential function such that

$C(t) = \sum_{i=1}^{n} a_i exp\,(\frac{-t}{\tau_i})$ satisfying $\sum_{i=1}^{n} a_i = 1$, where n=2 for our case.

Analytical Fourier transform of the autocorrelation function yields the spectral density function

$J(\omega) = \sum_{i=1}^{n} \frac{a_i\tau_i}{1+\omega^2\tau_i^2}$.

^{15}N spin relaxation parameters are calculated as linear combinations of J(ω) sampled at the eigenfrequencies of the spin system:

$$R_1 = \frac{0.1\mu_0^2\gamma_{1H}^2\gamma_{15N}^2\hbar^2}{(4\pi)^2/r_{NH}^6}[J(\omega_{1H}-\omega_{15N}) + 3J(\omega_{15N}) + 6J(\omega_{1H}+\omega_{15N})] + \left(\frac{2}{15}\right)\omega_N^2(\sigma_\parallel - \sigma_\perp)^2[J(\omega_{15N})]$$

$$R_2 = \frac{0.05\mu_0^2\gamma_{1H}^2\gamma_{15N}^2\hbar^2}{(4\pi)^2/r_{NH}^6}[4J(0) + J(\omega_{1H}-\omega_{15N}) + 3J(\omega_{15N}) + 6J(\omega_{1H}) + 6J(\omega_{1H}+\omega_{15N})] + \left(\frac{1}{45}\right)\omega_N^2(\sigma_\parallel - \sigma_\perp)^2[3J(\omega_{15N}) + 4J(0)]$$

$$NOE = 1 + \{\frac{0.1\mu_0^2\gamma_{1H}^3\gamma_{15N}\hbar^2}{(4\pi)^2/r_{NH}^6}[6J(\omega_{1H}+\omega_{15N}) - J(\omega_{1H}-\omega_{15N})]\left(\frac{1}{R_1}\right)\}$$

In above equations, μ_0 is the permeability of free space, γ_i is gyromagnetic ratio of the spin i, $\hbar$ is reduced Planck’s constant, $\sigma_\parallel$ and $\sigma_\perp$ are the parallel and perpendicular components of the axially symmetric ^{15}N chemical shift tensor, respectively. $\sigma_\parallel - \sigma_\perp$ is taken as -163 ppm (Yao et al., 2010), internuclear ^{1}H -^{15}N distance, r_{NH}, is taken as 1.02 Å and 850 MHz ^{1}H Larmor frequency is assumed in the calculation of R_1, R_2 and NOE.

Supplemental References

Abascal, J.L., and Vega, C. (2005). A general purpose model for the condensed phases of water: TIP4P/2005. J Chem Phys *123*, 234505.

Berendsen, H.J.C., Vanderspoel, D., and Vandrunen, R. (1995). Gromacs - a Message-Passing Parallel Molecular-Dynamics Implementation. Comput Phys Commun *91*, 43-56.

Best, R.B., Buchete, N.V., and Hummer, G. (2008). Are current molecular dynamics force fields too helical? Biophys J *95*, L07-09.

Bonomi, M., Branduardi, D., Bussi, G., Camilloni, C., Provasi, D., Raiteri, P., Donadio, D., Marinelli, F., Pietrucci, F., Broglia, R.A.*, et al.* (2009). PLUMED: A portable plugin for free-energy calculations with molecular dynamics. Comput Phys Commun *180*, 1961-1972.

Bonomi, M., and Parrinello, M. (2010). Enhanced sampling in the well-tempered ensemble. Phys Rev Lett *104*, 190601.

Bussi, G., Gervasio, F.L., Laio, A., and Parrinello, M. (2006). Free-energy landscape for beta hairpin folding from combined parallel tempering and metadynamics. J Am Chem Soc *128*, 13435-13441.

Delaglio, F., Grzesiek, S., Vuister, G.W., Zhu, G., Pfeifer, J., and Bax, A. (1995). NMRPipe: a multidimensional spectral processing system based on UNIX pipes. J Biomol NMR *6*, 277-293.

Essmann, U., Perera, L., Berkowitz, M.L., Darden, T., Lee, H., and Pedersen, L.G. (1995). A Smooth Particle Mesh Ewald Method. Journal of Chemical Physics *103*, 8577-8593.

Farrow, N.A., Zhang, O.W., Szabo, A., Torchia, D.A., and Kay, L.E. (1995). Spectral Density-Function Mapping Using N-15 Relaxation Data Exclusively. Journal of Biomolecular Nmr *6*, 153-162.

Fawzi, N.L., Ying, J., Torchia, D.A., and Clore, G.M. (2010). Kinetics of amyloid beta monomer-to-oligomer exchange by NMR relaxation. J Am Chem Soc *132*, 9948-9951.

Hess, B., Kutzner, C., van der Spoel, D., and Lindahl, E. (2008). GROMACS 4: Algorithms for Highly Efficient, Load-Balanced, and Scalable Molecular Simulation. J Chem Theory Comput *4*, 435-447.

Kjaergaard, M., Brander, S., and Poulsen, F.M. (2011). Random coil chemical shift for intrinsically disordered proteins: effects of temperature and pH. J Biomol NMR *49*, 139-149.

Kjaergaard, M., and Poulsen, F.M. (2011). Sequence correction of random coil chemical shifts: correlation between neighbor correction factors and changes in the Ramachandran distribution. J Biomol NMR *50*, 157-165.

Lee, W., Tonelli, M., and Markley, J.L. (2015). NMRFAM-SPARKY: enhanced software for biomolecular NMR spectroscopy. Bioinformatics *31*, 1325-1327.

Papaleo, E., Sutto, L., Gervasio, F.L., and Lindorff-Larsen, K. (2014). Conformational Changes and Free Energies in a Proline Isomerase. J Chem Theory Comput *10*, 4169-4174.

Prakash, M.K., Barducci, A., and Parrinello, M. (2011). Replica Temperatures for Uniform Exchange and Efficient Roundtrip Times in Explicit Solvent Parallel Tempering Simulations. J Chem Theory Comput *7*, 2025-2027.

Rost, B., and Sander, C. (1993). Prediction of Protein Secondary Structure at Better Than 70-Percent Accuracy. Journal of Molecular Biology *232*, 584-599.

Sugita, Y., and Okamoto, Y. (1999). Replica-exchange molecular dynamics method for protein folding. Chem Phys Lett *314*, 141-151.

Sutto, L., and Gervasio, F.L. (2013). Effects of oncogenic mutations on the conformational free-energy landscape of EGFR kinase. Proc Natl Acad Sci U S A *110*, 10616-10621.

Tropea, J.E., Cherry, S., and Waugh, D.S. (2009). Expression and purification of soluble His(6)-tagged TEV protease. Methods Mol Biol *498*, 297-307.

Vuister, G.W., and Bax, A. (1993). Quantitative J correlation: a new approach for measuring homonuclear three-bond J(HNH.alpha.) coupling constants in 15N-enriched proteins. Journal of the American Chemical Society *115*, 7772-7777.

Yao, L., Grishaev, A., Cornilescu, G., and Bax, A. (2010). The impact of hydrogen bonding on amide 1H chemical shift anisotropy studied by cross-correlated relaxation and liquid crystal NMR spectroscopy. J Am Chem Soc *132*, 10866-10875.